

Analytical Methods

Accepted Manuscript



This is an *Accepted Manuscript*, which has been through the Royal Society of Chemistry peer review process and has been accepted for publication.

Accepted Manuscripts are published online shortly after acceptance, before technical editing, formatting and proof reading. Using this free service, authors can make their results available to the community, in citable form, before we publish the edited article. We will replace this *Accepted Manuscript* with the edited and formatted *Advance Article* as soon as it is available.

You can find more information about *Accepted Manuscripts* in the [Information for Authors](#).

Please note that technical editing may introduce minor changes to the text and/or graphics, which may alter content. The journal's standard [Terms & Conditions](#) and the [Ethical guidelines](#) still apply. In no event shall the Royal Society of Chemistry be held responsible for any errors or omissions in this *Accepted Manuscript* or any consequences arising from the use of any information it contains.

1
2
3
4 **Near Infrared Fluorescence-Magnetic Resonance Dual-Modal**
5
6 **Imaging with Cy5-Labeled, Gd-Al Co-Doped Mesoporous Silica**
7
8
9 **Nanoparticles**

10
11 Ai Gao¹, Dan Zhang^{1,2}, Xue-Bo Yin^{1,*}

12
13 ¹ Research Center for Analytical Sciences, College of Chemistry, Nankai University,
14
15 State Key Laboratory of Medicinal Chemical Biology, Tianjin Key Laboratory of
16
17 Biosensing and Molecular Recognition, and Collaborative Innovation Center of
18
19 Chemical Science and Engineering (Tianjin), Tianjin, 300071, China
20
21

22
23
24 ² Tianjin Key Laboratory of Aquatic Science and Technology, School of
25
26 Environmental and Municipal Engineering, Tianjin Chengjian University, Tianjin,
27
28 300384, China
29
30

31
32
33 * E-mail: xbyin@nankai.edu.cn; Fax: (86) 22 2350 3034
34
35
36
37
38
39
40
41
42
43
44
45
46
47
48
49
50
51
52
53
54
55
56
57
58
59
60

Abstract

To obtain comprehensive information and to compensate the limits of individual modalities in molecular imaging, the research on dual-modal imaging probes (DMIPs) attracts much interest. Here, we reported a reliable and facile procedure to prepare near infrared fluorescence (NIRF)-magnetic resonance (MR) DMIPs using Cy5-labeled, Gd-Al co-doped mesoporous silica nanoparticles (MSNs). Amine-modified, Gd-Al co-doped MSNs were first synthesized through one-step co-condensation. Cy5-NHS ester was then coupled to the amino groups to produce the DMIPs, which were denoted as Gd-Al@MSNs-Cy5. High intensity of NIRF and relaxation rate ($17.7 \text{ mM}^{-1}\text{s}^{-1}$) were observed. Featuring the lower background, the deeper penetration depth, the cutting-edge NIRF imaging was achieved. Moreover, larger surface area of MSNs could be modified with more NIRF probes, Cy5, for improved NIRF. Following the Solomon–Bloembergen–Morgan theory, enhanced MR performance was illustrated by the relaxation rate because MSNs have porous structure that enables access of water into the interior, and co-doping with Al in the MSNs promotes the doped amount of Gd. The exchange rate of water is much more accelerated through doping Gd and Al since disordered pore arrangement is found in Gd-Al co-doped MSNs. The DMIPs in saline were injected into mice through tail vein for imaging and basic pharmacokinetics study. They were excreted by the stomach and intestine in 3 h, a circulation time long enough for imaging. Thus, Gd-Al@MSNs-Cy5 is attractive in clinical NIRF-MR dual-modal imaging by integrating the biocompatibility of MSNs, the NIRF of Cy5, and the high MR response of Gd.

Keywords

Fluorescence Imaging; Magnetic Resonance Imaging; Dual-Modality Imaging; Gadolinium; Mesoporous Silica

Introduction

Molecular imaging reveals the generation, development, and metastasis of tumor, allowing precise delivering of medicine and dynamic monitoring of personalized treatment.^{1,2} To obtain comprehensive information and to compensate the limits of individual modalities in clinical diagnostics, the dual-modal imaging probes (DMIPs) have been rapidly developed.³ Fluorescence and magnetic resonance (MR) imaging are considered to be a complementary pair. Fluorescence imaging shows high sensitivity but poor spatial resolution with relatively moderate tissue penetration depth, while MR imaging is unlimited in penetration depth and prominent in spatial resolution yet lacks sensitivity.⁴ The first fluorescence-MR DMIPs was introduced by Huber et al. in 1998, where rhodamine derivatives and Gd lay the foundations for fluorescence and MR imaging, respectively.⁵ However, several issues impede the real bio-medical applications of the fluorescence-MR DMIPs, including but not restricted to (1) high background and rather limited penetration depth of fluorescence; (2) insufficient MR imaging contrast agent payload; (3) inadequate surface areas to be modified or to contact with water in nanoparticle-based DMIPs; and (4) complex design and laborious preparation of DMIPs.

Traditional fluorescence imaging is subjected to auto-fluorescence and low penetration depth of the tissue, leading to high level of background and inaccuracy. Whereas longer wavelength light, such as near infrared fluorescence (NIRF) that ranges from 650 to 1350 nm in wavelength, is less absorbed or scattered by tissues.⁶ Featuring the lower background, deeper penetration depth, and higher spatial resolution,^{7, 8} the cutting-edge NIRF imaging overmatches the other optical techniques. Currently developed NIRF imaging probes can be classified into two categories: Stokes type and anti-Stokes type (up-conversion). The later refers to precious rare earth elements doped nanoparticles,⁹ while the former is more common, mainly include fluorescent proteins,¹⁰ organic dyes,¹¹ metallorganics,¹² and nanometerials, e.g., gold clusters,¹³ silver clusters,¹⁴ and quantum dots etc.¹⁵ For biodegradability, non-toxicity, convenient labeling concern, organic NIRF dyes have been widely used, like Cy5,¹⁶ Cy5.5,¹⁷ and indocyanine green.¹⁸

1
2
3
4
5
6
7
8
9
10
11
12
13
14
15
16
17
18
19
20
21
22
23
24
25
26
27
28
29
30
31
32
33
34
35
36
37
38
39
40
41
42
43
44
45
46
47
48
49
50
51
52
53
54
55
56
57
58
59
60

Unlike many other modalities, the 3D magnetic resonance (MR) imaging is both non-radiation and non-invasive. It is especially valuable in visualizing soft tissues. MR images are created by recording the demagnetization (relaxation) rates of magnetized protons of water in different chemical environment, then converting them into grayscale images.¹⁹ Since the chemical environments in different tissues are often dissimilar, the contrast is formed between adjacent tissues. The contrast agent will further enhance the inherent contrast by shortening the relaxation course of nearby protons. Examples are paramagnetic metal complexes or species containing Gd²⁰ or Mn²¹ and superparamagnetic iron oxide.²² In particular, Gd-containing species are intensely studied because Gd³⁺ has up to seven unpaired electrons, a large magnetic moment is therefore expected. According to Solomon–Bloembergen–Morgan theory, the relaxation time decreases with increasing hydration number of Gd, accelerating the exchange rate of the inner shell and outer shell water, and enlarging the molecular weight of Gd compounds.²³ Besides, multiple Gd centers in one molecular (unit) help quick relaxation.²⁴ Only one water binding site is left in two approved contrast agents in clinical MR imaging, Gd-DOTA and Gd-DTPA. New ligands with more than one site need careful design and synthesis.²⁵ An alternative strategy to design improved Gd-contained contrast agents is loading them on nanoparticle carriers, increasing the molecular weight and the payload of Gd complexes simultaneously.^{26,27}

New methodologies enable functional nanoparticles synthesized with controllable morphology and structure.²⁸ Modifying the surface alters their physical properties and expands their functions, which is the basis of theranostics.²⁹ DMIPs are preferentially built on nanoparticles with respect to the enhanced permeability and retention effect that makes the tumor passive-targetable, thus precise imaging and drug-delivery become practical.³⁰ Nevertheless, post-linking of Gd complexes on solid nanoparticles result in limited outer surface labelling, while doping Gd complexes in the inner affect the exchange rate of water. We therefore explore nanoparticles with substantial Gd-doped, without perturbing the exchange rate of water simultaneously.³¹ The biocompatible mesoporous silica nanoparticles (MSNs)

1
2
3 are the best, as their porous structure enables access of water into the interior, along
4 with larger surface area that can be modified. Previous literatures proved that
5 co-doping with Al in the MSNs promotes the doped amount of Gd.^{32,33} Because Al³⁺
6 is similar to Si⁴⁺ in size; the negative charge is produced when Al³⁺ is incorporated
7 into the MSNs during their formation. Gd³⁺ as a counter-ion is loaded by
8 ion-exchange to balance the charge. Importantly, the exchange rate of water is much
9 more accelerated through doping Gd and Al, since disordered pore arrangement is
10 found in Gd-Al doped MSNs, where the interconnection of pores facilitate the free
11 diffusion of water.^{33,34} In our previous work, Gd-Al doped MSNs was integrated to
12 Ru(bpy)₃²⁺ via ion-exchange procedure as fluorescence-MR DMIPs.³³ However,
13 Ru(bpy)₃²⁺ suffers from low fluorescence efficiency and the ion-exchanged
14 Ru(bpy)₃²⁺ may be leaked.

15
16 Here, we report a reliable and facile procedure to prepare NIRF-MR DMIPs
17 using Cy5-labeled, Gd-Al co-doped MSNs (Gd-Al@MSNs-Cy5). Different to the
18 simple MSNs in our previous work,³³ amine-modified, Gd-Al co-doped MSNs
19 (Gd-Al@MSNs-NH₂) were first synthesized through one-step co-condensation.
20 Cy5-NHS ester was then coupled to the amino groups to produce the DMIPs.
21 Different to the previous DMIPs,^{33,35,36} Gd-Al@MSNs-Cy5 address the four issues
22 well. Highly intensive NIRF from Cy5 enjoy the low background and high
23 penetration depth. While co-doped Al increases the loading of Gd ions, the
24 mesoporous structure enhances the exchange of water molecule, so high relaxation
25 rate and contrast efficiency were observed. Importantly, mesoporous silica provides a
26 biocompatible platform to integrate the signal sources, Gd ions and Cy5, with a
27 simple preparation procedure and high yield. All of the properties were validated by
28 the imaging and basic pharmacokinetics study with mice as model through tail vein
29 injection.
30
31
32
33
34
35
36
37
38
39
40
41
42
43
44
45
46
47
48
49
50
51
52
53
54
55
56
57
58
59
60

Experimental

Chemicals and apparatus

Cetyltrimethyl ammonium bromide (CTAB), diethanolamine (DEA), and (3-aminopropyl)triethoxysilane (APTES) were purchased from J&K Scientific. Tetraethoxysilane (TEOS) was from Concord, Tianjin, China. Aluminum chloride (AlCl_3) and gadolinium oxide (Gd_2O_3) were from Aladdin Industrial. Absolute anhydrous N,N-Dimethylformamide (DMF) was from Heowns, Tianjin, China. Cyanine5 NHS ester (Cy5-NHS) was obtained from Fanbo, Beijing, China. GdCl_3 was produced by the reaction of Gd_2O_3 with hydrochloric acid. All other reagents were analytical grade. Ultrapure water was used throughout the experiment.

Fourier transform infrared (FTIR) spectra were recorded by a Nicolet Magna 560 IR spectrometer. Transmission electron microscopy (TEM) images were captured by an FEI Tecnai G2 transmission electron microscope. N_2 adsorption-desorption outcomes were analyzed with a Micromeritics TriStar 3000 surface area and pore size analyzer. Elemental contents were determined by Thermo IRIS Intrepid II XSP inductively coupled plasma atomic emission spectroscopy (ICP-AES). Fluorescence was recorded using a Hitachi FL-4500 fluorescence spectrophotometer, NIRF imaging was performed by a Kodak *in vivo* imaging systems FX. Relaxation time and MR imaging were executed with a Huantong (Shanghai, China) HT-MRSI60-60 KY MR imaging scanner.

Synthesis of Gd-Al@MSNs-NH₂

The synthesis of Gd-Al@MSNs-NH₂ resembles the previous works.³⁷⁻⁴⁰ After dissolving 0.29 g CTAB (0.79 mmol) in a mixture of 6.4 mL water (0.36 mol) and 0.92 mL ethanol (0.02 mol) by sonication for 10 min, 0.05 g DEA (0.48 mol) was added and heated to 60 °C. TEOS was added drop-wise under vigorous stirring for 10 min (supplementary information, Table S1). Then, 0.20 mL of a GdCl_3 (0.13 mmol) and AlCl_3 (0.06 mmol) solution was added, and the reaction proceeded for 1 h. An equal volume of TEOS and APTES was added together and reacted for another 2 h period to integrate amine group in the exterior and interior surface. Subsequently, the

1
2
3 reaction system was allowed to cool, and the nanoparticles, Gd-Al@MSNs-NH₂, were
4 washed with ethanol for three times. The collected were refluxed in an acidified
5 ethanol for 6 h to remove CTAB, and finally dispersed in 10 mL ethanol after
6 washing.
7
8
9

10 Labelling Cy5 on Gd-Al@MSNs-NH₂

11
12
13 25 mg dry Gd-Al@MSNs-NH₂ was dispersed in 8 mL anhydrous DMF containing 1
14 mg Cy5-NHS and 80 μ L tripropylamine. The mixture was stirred in dark at room
15 temperature for 24 h. Then the nanoparticles, Gd-Al@MSNs-Cy5, were washed with
16 ethanol for five times and dispersed in 5 mL water.
17
18
19
20
21
22
23

24 Toxicity of Gd-Al@MSNs-Cy5

25
26 The cell viability was recorded after HepG2 cells were incubated with
27 Gd-Al@MSNs-Cy5 at different concentrations using a standard MTT
28 [3-(4,5-dimethylthiazol-2-yl)-2,5-diphenyltetrazolium bromide] assay to test the
29 toxicity of Gd-Al@MSNs-Cy5. The cells were incubated to 96-well culture plates at a
30 density of 5×10^3 cells per well in culture medium. Gd-Al@MSNs-Cy5 and Gd³⁺ ions
31 at the concentrations from 0 to 20 mg L⁻¹ (based on Gd³⁺) were introduced to the
32 medium and incubated HepG2 cells for 24 h. MTT solution (20 mL, 0.1 mg) were
33 added to each well and the cells were incubated for another 4 h. N,N'-dimethyl
34 sulfoxide (150 μ L) was used to completely liberate the formazan crystals. The
35 absorbance at 490 nm was measured for the calculation of the cell viability.
36
37
38
39
40
41
42
43
44
45
46

47 Fluorescence measurement and NIRF imaging

48
49 Steady-state fluorescence was excited with 630 nm wavelength at room temperature
50 using a Hitachi FL-4500 fluorescence spectrophotometer. The excitation source is a
51 450 W xenon lamp coupled to a monochromator with a 1200 groves/mm grating.
52 During *in vivo* and *ex vivo* imaging, female nude mice (6 weeks old, *BALB/c-nu*) were
53 initially anesthetized with 4 % chloral hydrate in a dosage of 8.25 μ L g⁻¹, and further
54 anesthetized with 2 % chloral hydrate. Then, 200 μ L of 10 mg mL⁻¹
55
56
57
58
59
60

1
2
3 Gd-Al@MSNs-Cy5 saline was injected through tail vein of the mice. The
4
5 fluorescence was excited at 625 nm wavelength and collected at 690 nm. The black
6
7 and white fluorescence images were superimposed for better visualization. At last, the
8
9 mice were sacrificed and dissected to image the individual organs. The mice were
10
11 obtained from the Institute of Hematology & Hospital of Blood Diseases, Chinese
12
13 Academy of Medical Sciences & Peking Union Medical College with the license No.
14
15 SCXK-2004-001, Tianjin, China. The mice have free access to solid rodent chow and
16
17 water. All experimental protocols using animals were also approved by the
18
19 Institutional Animal Care Committee of Nankai University.

22 Relaxation time measurement and MR imaging

23
24 Relaxation time was measured on an MR imaging scanner (1.2 T, 30 °C) using the
25
26 inversion-recovery method. *In vitro* T1-weighted phantom imaging and *in vivo* MR
27
28 imaging (using female Kunming mice, 8 weeks old, outbred stock) was based on
29
30 spin-echo method. 300 μ L of 10 ng mL⁻¹ saline solution of Gd-Al@MSNs-Cy5 was
31
32 injected into the mice through the tail vein. MR imaging was conducted using a
33
34 T1-weighted sequence with TR/TE = 200/14 ms, FOV = 75 mm×75 mm, flip angle =
35
36 60 °, number of excitation = 3.

39 **Results and discussion**

41 Synthesis of the DMIPs

42
43 MSNs were prepared to load with Cy5 and Gd³⁺ for the synthesis of the NIRF-MR
44
45 DMIPs. Hydrolyzation and co-condensation of TEOS and APTES are extensively
46
47 reported to directly produce NH₂-functional MSNs with simple procedure and high
48
49 yield.^{35,36} Precipitation is avoided and amine groups are homogeneously distributed,
50
51 forming Gd-Al@MSNs-NH₂ in one step.⁴⁰ The impact of the amount of both TEOS
52
53 and APTES on the surface charge of the Gd-Al@MSNs-NH₂ is summarized in Table
54
55 S1. More APTES, more positive charges, which means more amino groups are
56
57 formed on the Gd-Al@MSNs-NH₂. The increase of absolute value of zeta-potential
58
59 favors the dispersion and stability of the Gd-Al@MSNs-NH₂. The composition and
60

1
2
3 ratio in Sample 4 in Table 1 is the optimal, considering the stability, the Gd-loading
4 amount, the relaxation rate, and the number of amines that coupled with Cy5. The
5 Zeta potential of the Gd-Al@MSNs-Cy5 was tested and -7.8 mV, which is lower than
6 that from mesoporous silica nanoparticles because of the existence of amino groups.
7 The amine group-modified mesoporous structure provides a platform to integrate Gd
8 ions and Cy5 for MR and NIRF dual-response.
9
10
11
12
13
14
15

16 Morphology and structure of the DMIPs

17 The morphology and microstructure of the DMIPs were characterized. All
18 nanoparticles appeared to be uniform spheres as shown in the TEM images in Fig. 1.
19 The average diameters of Gd-Al@MSNs-NH₂ and Gd-Al@MSNs-Cy5 were ca. 57
20 nm. In addition, mesoporous structure of the intragranular network of the
21 nanoparticles was observed clearly (Fig. 1B). Since post-grafting of Cy5 to the
22 surfaces and pores would not influence the dispersion and the structure of the
23 nanoparticles, the exchange rate of water between the surroundings and the internals
24 of nanoparticles was not interfered, thus maintaining the high relaxivity.
25
26
27
28
29
30
31
32

33 The mesoporous structure of Gd-Al@MSNs-NH₂ was further investigated by
34 XRD and N₂ adsorption-desorption test. Doping with Al³⁺ decrease the size of the
35 MSNs as a result of pH decrease of reaction system after addition of Al³⁺.^{33, 38}
36 Moreover, Al³⁺ co-dopant could greatly reduce the structural stress within the silicate
37 matrix, induced by the charge and size mismatch of the trivalent Gd³⁺, which
38 therefore disrupted the order of the MSNs structure.⁴¹ Consequently, the XRD peaks
39 of Gd-Al@MSNs-NH₂ went broaden and some of them disappeared. Long-range
40 order MSNs like hexagonal MCM-41 are typically characterized to exhibit three sharp
41 Bragg peaks (100), (110), (200) at two-theta angle less than 5°, while only one broad,
42 weak peak at low angles indexed as (100) diffractions of Gd-Al@MSNs-NH₂ was
43 found, as shown in Fig. S1A (Supplementary Information). N₂ adsorption-desorption
44 of Gd-Al@MSNs-NH₂ reflects their textural properties (Fig. S1B). A type IV
45 isotherm with an evident hysteresis loop at high pressures account for the mesoporous
46 nature and the small size of Gd-Al@MSNs-NH₂. Using Brunauer-Emmett-Teller test,
47
48
49
50
51
52
53
54
55
56
57
58
59
60

1
2
3 the surface area is $882.7 \text{ m}^2\text{g}^{-1}$, and total pore volume is $1.2 \text{ cm}^3 \text{ g}^{-1}$. The maximum
4 pore size is 2.5 nm (inset) based on Barrett-Joyner-Halenda (BJH) test. The BJH
5 model is based on Kelvin equation, $\ln p/p_0 = -2\sigma V_L \cos\theta / RT r_k$. The r_k obtained by
6 Kelvin equation plus the thickness of liquid film is the pore diameter. Small size and
7 large pores facilitate the loading of a substantial amount of Cy5 and the exchange of
8 water to maintain the high relaxivity. Based on the results above, Fig. 1C illustrated
9 the mesoporous structure with the co-doped Gd and Al as well as the labeled Cy5.
10

11
12 The conjugation of Cy5 with Gd-Al@MSNs-NH₂ was confirmed by the FTIR
13 spectra. As shown in Fig. S2a (supplementary information), the band between 3500
14 and 3200 cm^{-1} is assigned to the N-H stretching vibrations of primary amine; the
15 peaks near 1640 and 1560 cm^{-1} are the bending vibrations of primary amine, which
16 approve the existence of the amine group on Gd-Al@MSNs-NH₂. As amide
17 characteristic stretching vibrations appear at 1450 cm^{-1} (Fig. S2b), and there are two
18 sharp peaks at 1180 and 1130 cm^{-1} related to stretching vibration of aromatic sulfonic
19 acid groups on Cy5, so Cy5 is successfully linked to Gd-Al@MSNs-NH₂. The loading
20 content of Cy 5 was $4.17 \times 10^{-5} \text{ mol g}^{-1}$, which was calculated based on the
21 fluorescence intensity from the probe with the emission of Cy5 solution as standard.
22
23
24
25
26
27
28
29
30
31
32
33
34
35
36

37 Fluorescence property of the DMIPs

38
39 The optical properties of the Gd-Al@MSNs-Cy5 were investigated. While
40 Gd-Al@MSNs-Cy5 solution was cyan (Fig. 2A), NIRF emission was observed when
41 illuminated by 365 nm UV light (Fig. 2B). As shown in Fig. 2C, the maximum
42 emission wavelengths are 682 and 684 nm for Cy5 and Gd-Al@MSNs-Cy5,
43 respectively, under 630 nm excitation. The nearly identical wavelengths indicate the
44 luminescent property of Cy5 remained even Cy5 was linked to the MSNs. Strong
45 NIRF from Cy5 can increase the signal-to-noise ratio during *in vivo* fluorescence
46 imaging of the probe.
47
48
49
50
51
52
53
54

55 Relaxation property of the DMIPs

56
57 The content of Gd is a critical parameter of Gd-related contrast agents. When we
58
59
60

1
2
3 calculated longitudinal and the transverse relaxation rate, r_1 and r_2 , the precise
4 concentration of Gd is necessarily acquired. After Gd-Al@MSNs-Cy5 was dissolved
5 in nitric acid/hydrofluoric acid mixture, it was subsequently analyzed by ICP-AES to
6 quantify the amount of Gd and Al. Table 1 summarizes the amount of Gd and Al, and
7 the relaxation rate in different Gd-Al@MSNs-NH₂. It can be seen from Table S1 that
8 the amount of Gd and Al is decreased with increasing APTES. The negative charge is
9 produced when Al is incorporated into the MSNs, and Gd, as a counter-ion, is loaded
10 into the MSNs by ion-exchange to balance the charge.⁴² Simultaneously, the positive
11 charge formed during APTES hydrolysis, which balances part of the negative charge
12 generated by TEOS hydrolysis. Because APTES could lower the negative charge in
13 the reaction, the amount of Gd and Al in the MSNs is decreased. Sample 4 in Table 1
14 shows the highest relaxation property, with 17.3 mM⁻¹ s⁻¹ of longitudinal relaxation
15 rate, 4.1-fold higher than Gd-DTPA.³³ The probe's r_2/r_1 is ca 1.1, which is suitable as
16 a positive contrast agent. In general, r_2/r_1 less than 2 is common for T₁ contrast agent.
17²⁵ Therefore, DMIPs can be established using near-infrared dye linked Sample 4 in
18 Table S1.

19
20
21
22
23
24
25
26
27
28
29
30
31
32
33
34
35
36
37
38
39
40
41
42
43
44
45
46
47
48
49
50
51
52
53
54
55
56
57
58
59
60
The content of Gd and Al in Gd-Al@MSNs-Cy5 is 259.0 μmol g⁻¹ and 263.2
μmol g⁻¹, respectively, while the molar ratio of Al and Gd is 1.02, with r_1 of 17.7
mM⁻¹s⁻¹ and 1.1 of r_2/r_1 ratio. Compared with Sample 4, little influence was observed
when coupling of Cy5 on the surface of the pores and nanoparticles, indicating Cy5
cannot hinder the diffusion and exchange rate of water. The results in Fig. 2D and Fig.
2E illustrated that the as-prepared DMIPs is applicable in *in vivo* MR applications.

Stability of the DMIPs

The leakage of metal ions from 0.5 mg mL⁻¹ Gd-Al@MSNs-Cy5 in phosphate buffer
saline (PBS, pH 7.4) is measured by ICP-AES to illustrate the stability of DMIPs. The
DMIPs contained 2036 ppm Gd and 355 ppm Al (the limit of detection of Gd and Al
is 0.0154 ppm and 0.0174 ppm, respectively). No Gd or Al in the supernatant after
centrifugation was detected after one day, one week, and even one month. Any
leakage of Gd and Al from the DMIPs is avoided.

Gd³⁺ ions are toxic and often used in the form of complexes to reduce their toxicity. We tested the cell viability after being incubated with Gd-Al@MSNs-Cy5 probe and Gd ions with HepG2 cells as model. As shown in Figure S3, while the cell viability was almost the same around 100 % after incubated with Gd-Al@MSNs-Cy5 probe at different concentration, Gd³⁺ ions led to the gradually decreased cell viability with the increased concentration. Only 30 % of cell viability was observed at 20 mg L⁻¹ of Gd³⁺ ions. The above results confirmed the high biocompatibility of MSNs and less leakage of Gd³⁺ ions from the probe.

The fluorescence of pure PBS and the supernatant after centrifugation of Gd-Al@MSNs-Cy5 in PBS are measured, after one day, one week, and one month. The ratio of the intensity is 1:1.03:1.03:1.02, so less Cy5 is leaked, which contribute to the covalently coupling on the nanoparticles. The stability of fluorescence intensity and relaxation rate was also examined. The Gd-Al@MSNs-Cy5 were kept in suspension and stored away from light at 4 °C during the test. As illustrated in Fig. S4 (supplementary information), the fluorescence intensity and relaxation rate remained the same after 10 days.

NIRF imaging using the DMIPs

In vivo NIRF and MR imaging of mice using Gd-Al@MSNs-Cy5 was tested to show its bio-effects and imaging application. The *BALB/c* mice were injected with 200 μL colloidal saline of DMIPs at a concentration of 10 mg ml⁻¹ through the tail vein. Cy5-labeling is better than fluorescein or rhodamine-labeling, because its emission could only be weakly absorbed by the liver tissue so as to penetrate much more deeply.⁴³ As shown in Fig. 3, the NIRF image of the mice verifies the bright fluorescence could penetrate the body. We monitored the mice after injection in the period between 0.5 to 3 h (Fig. 3A). Strong emission was observed throughout the body after injection different to the low fluorescence efficiency of Ru(bpy)₃²⁺ used in our previous work.³³ By systematic circulation, the DMIPs gradually accumulated in the mononuclear phagocyte system like liver and spleen. Finally, most of the DMIPs were excreted by the stomach and intestines. 3 h later, mice were sacrificed and dissected to confirm the

1
2
3 bio-distribution of the DMIPs. As shown in Fig. 3B, high intensity of fluorescence
4 was observed from the stomach and the intestines, while no fluorescence were
5 detected from the heart and the lung. The DMIPs could be cleared from the mice,
6 since little were found in liver, spleen, and kidneys. The above results reveal
7 Gd-Al@MSNs-Cy5 can be used in *in vivo* NIRF imaging. Large surface area of
8 MSNs can load more Cy5 that emits strong fluorescence, and the NIRF from Cy5
9 shows deep tissue penetration capability.
10
11
12
13
14
15
16
17

18 MR imaging using the DMIPs

19
20 The results of MR imaging were in accordance with that of the NIRF imaging (Fig. 4).
21 The 30 g female Kunming mice were injected with 300 μ L colloidal saline of
22 Gd-Al@MSNs-Cy5 (25.6 μ mol kg^{-1} of Gd), and the T1-weight MR images at
23 pre-injection through tail-vein (blank), post-injection at 0.5, 1, 2, and 3 h, were
24 recorded. The MR signal was first enhanced at the liver as it was the main uptake
25 organ of the DMIPs. During the next 3 h, evident contrast appeared at the intestines.
26 Hence, it is speculated that after blood circulation, the DMIPs will accumulate in the
27 liver, which are then excreted by the kidneys or enter the stomach then reach the
28 intestines. Similarly, no signal enhancement was spotted in heart and lung. The above
29 results reveal that Gd-Al@MSNs-Cy5 can be used in *in vivo* MR imaging. Our
30 method of synthesizing the DMIPs allows sufficient Gd payload, and the inherent
31 porous structure of Gd and Al co-doped MSNs further facilitate water diffusion into
32 the inner of the DMIPs, both of which are beneficial for Gd-Al@MSNs-Cy5 in *in vivo*
33 MR imaging.
34
35
36
37
38
39
40
41
42
43
44
45
46
47
48

49 Expansibility of the DMIPs

50 The DMIPs presented herein overcome several limitations in nanoparticle-based
51 dual-modal imaging. They are simple and reliable in design and preparation. In
52 addition, their functions can be further expanded. Some diseases like cancer
53 abundantly express biomarkers, and antibodies⁴⁴ along with nucleic acid aptamers
54 recognized them have been identified.⁴⁵ On another aspect, diverse therapeutic
55
56
57
58
59
60

1
2
3 methods, including photodynamic therapy, photothermal therapy, chemotherapy,
4 radiotherapy, etc., are originated with corresponding molecules or nanoparticles.⁴⁶
5
6 Smart theranostic agents can be synthesized based on our work herein, integrating the
7 abilities of (1) actively and selectively multi-valency targeting of tumor by coupling
8 various antibodies and/or aptamers on the large surface of Gd-Al@MSNs-Cy5; (2)
9 cooperative treatment of cancer by linking and/or entrapping therapeutic-effective
10 molecules or nanoparticles to Gd-Al@MSNs-Cy5.
11
12

13 14 15 16 17 **Conclusions**

18 In this paper, NIRF-MR DMIPs using Cy5-labeled, Gd-Al co-doped MSNs were
19 constructed reliably and facily. Detailed design and characterization of the excellent
20 properties of NIRF and MR were demonstrated both *in vitro* and *in vivo*, suggesting
21 Gd-Al@MSNs-Cy5 were an attractive candidate in clinical NIRF-MR imaging.
22 Furthermore, it is possible to expand the functions of Gd-Al@MSNs-Cy5.
23 Overcoming several issues common in dual-modal imaging based on functional
24 nanoparticles, our work herein gives solutions to effectively enhance the fluorescence
25 and MR signal intensities, and simplifies the design and preparation procedure
26 simultaneously.
27
28
29
30
31
32
33
34
35
36

37 38 **Acknowledgements**

39 This work was supported by National Natural Science Foundation of China (No.
40 21375064 and 21435001), 973 projects (No. 2015CB932001), Tianjin Natural
41 Science Foundation (No. 15ZCZDSF00060), and Research Fund for the Doctoral
42 Program of Higher Education (No. 20130031110016).
43
44
45
46
47
48
49
50
51
52
53
54
55
56
57
58
59
60

References

1. T. Florio and F. Barbieri, *Drug Discov. Today*, 2012, **17**, 1103-1110.
2. Z. Jia, D. Geng, T. Xie, J. Zhang and Y. Liu, *J. Clin. Neurosci.*, 2012, **19**, 820-823.
3. S. S. Kelkar and T. M. Reineke, *Bioconjugate Chem.*, 2011, **22**, 1879-1903.
4. B. A. Smith and B. D. Smith, *Bioconjugate Chem.*, 2012, **23**, 1989-2006.
5. M. M. Huber, A. B. Staubli, K. Kustedjo, M. H. B. Gray, J. Shih, S. E. Fraser, R. E. Jacobs and T. J. Meade, *Bioconjugate Chem.*, 1998, **9**, 242-249.
6. H. Kobayashi, M. Ogawa, R. Alford, P. L. Choyke and Y. Urano, *Chem. Rev.*, 2010, **110**, 2620-2640.
7. T. Furuta, M. Nakada, K. Misaki, Y. Sato, Y. Hayashi, Y. Nakanuma and J.-i. Hamada, *Brain Tumor Pathol.*, 2014, **31**, 32-39.
8. A. D. Norden, G. S. Young, K. Setayesh, A. Muzikansky, R. Klufas, G. L. Ross, A. S. Ciampa, L. G. Ebbeling, B. Levy, J. Drappatz, S. Kesari and P. Y. Wen, *Neurology*, 2008, **70**, 779-787.
9. J. Zhou, N. Shirahata, H.-T. Sun, B. Ghosh, M. Ogawara, Y. Teng, S. Zhou, R. G. S. Chu, M. Fujii and J. Qiu, *J. Phys. Chem. Lett.*, 2013, **4**, 402-408.
10. D. Yu, W. C. Gustafson, C. Han, C. Lafaye, M. Noirclerc-Savoie, W.-P. Ge, D. A. Thayer, H. Huang, T. B. Kornberg, A. Royant, L. Y. Jan, Y. N. Jan, W. A. Weiss and X. Shu, *Nat. Commun.*, 2014, **5**, 3626.
11. C.-S. Yeh, C.-H. Su, W.-Y. Ho, C.-C. Huang, J.-C. Chang, Y.-H. Chien, S.-T. Hung, M.-C. Liao and H.-Y. Ho, *Biomaterials*, 2013, **34**, 5677-5688.
12. H. Ke, H. Wang, W.-K. Wong, N.-K. Mak, D. W. J. Kwong, K.-L. Wong and H.-L. Tam, *Chem. Commun.*, 2010, **46**, 6678-6680.
13. H. Hu, P. Huang, O. J. Weiss, X. Yan, X. Yue, M. G. Zhang, Y. Tang, L. Nie, Y. Ma, G. Niu, K. Wu and X. Chen, *Biomaterials*, 2014, **35**, 9868-9876.
14. C. Wang, L. Xu, X. Xu, H. Cheng, H. Sun, Q. Lin and C. Zhang, *J. Colloid Interface Sci.*, 2014, **416**, 274-279.
15. I. Hocaoglu, F. Demir, O. Birer, A. Kiraz, C. Sevrin, C. Grandfils and H. Y. Acar, *Nanoscale*, 2014, **6**, 11921-11931.
16. X. He, J. Chen, K. Wang, D. Qin and W. Tan, *Talanta*, 2007, **72**, 1519-1526.

17. L. Jiang, Q. Zhou, K. Mu, H. Xie, Y. Zhu, W. Zhu, Y. Zhao, H. Xu and X. Yang, *Biomaterials*, 2013, **34**, 7418-7428.
18. M. A. Jarzabek, P. C. Huszthy, K. O. Skaftnesmo, E. McCormack, P. Dicker, J. H. M. Prehn, R. Bjerkvig and A. T. Byrne, *Mol. Imaging*, 2013, **12**, 161-172.
19. P. Reimer, P. M. Parizel, J. F. M. Meaney and F. A. Stichnoth, *Clinical MR Imaging: A Practical Approach*, 3rd edn., Springer, 2010.
20. J. Tang, Y. Sheng, H. Hu and Y. Shen, *Prog. Polym. Sci.*, 2013, **38**, 462-502.
21. M. Kueny-Stotz, A. Garofalo and D. Felder-Flesch, *Eur. J. Inorg. Chem.*, 2012, 1987-2005.
22. N. Lee and T. Hyeon, *Chem. Soc. Rev.*, 2012, **41**, 2575-2589.
23. A. J. L. Villaraza, A. Bumb and M. W. Brechbiel, *Chem. Rev.*, 2010, **110**, 2921-2959.
24. C. Shen and E. J. New, *Curr. Opin. Chem. Biol.*, 2013, **17**, 158-166.
25. P. Caravan, J. J. Ellison, T. J. McMurry and R. B. Lauffer, *Chem. Rev.*, 1999, **99**, 2293-2352.
26. F. Chen, W. Bu, S. Zhang, J. Liu, W. Fan, L. Zhou, W. Peng and J. Shi, *Adv. Funct. Mater.*, 2013, **23**, 298-307.
27. Y. Liu and N. Zhang, *Biomaterials*, 2012, **33**, 5363-5375.
28. L. H. Tan, H. Xing and Y. Lu, *Accounts Chem. Res.*, 2014, **47**, 1881-1890.
29. Z. Cheng, A. Al Zaki, J. Z. Hui, V. R. Muzykantov and A. Tsourkas, *Science*, 2012, **338**, 903-910.
30. H. Maeda, *J. Control. Release*, 2012, **164**, 138-144.
31. Z. Cheng, D. L. J. Thorek and A. Tsourkas, *Angew. Chem.-Int. Edit.*, 2010, **49**, 346-350.
32. A. J. Silversmith, N. T. T. Nguyen, B. W. Sullivan, D. M. Boye, C. Ortiz and K. R. Hoffman, *J. Lumines.*, 2008, **128**, 931-933.
33. D. Zhang, A. Gao, Y. Xu, X.-B. Yin, X.-W. He and Y.-K. Zhang, *Analyst*, 2014, **139**, 4613-4619.
34. N. M. K. Tse, D. F. Kennedy, N. Kirby, B. A. Moffat, T. M. Hinton, B. W. Muir, R. A. Caruso and C. J. Drummond, *J. Mat. Chem. B*, 2013, **1**, 1219-1222.
35. L. Tang, X. Yang, L. W. Dobrucki, I. Chaudhury, Q. Yin, C. Yao, S. Lezmi, W. G. Helferich, T. M. Fan and J. Cheng, *Angew. Chem.-Int. Edit.*, 2012, **51**, 12721-12726.
36. D. W. Hwang, H. Y. Ko, J. H. Lee, H. Kang, S. H. Ryu, I. C. Song, D. S. Lee and S. Kim, *J. Nucl. Med.*, 2010, **51**, 98-105.
37. J. Kobler, K. Moeller and T. Bein, *ACS Nano*, 2008, **2**, 791-799.
38. Z.-A. Qiao, L. Zhang, M. Guo, Y. Liu and Q. Huo, *Chem. Mat.*, 2009, **21**, 3823-3829.

- 1
2
3
4
5
6
7
8
9
10
11
12
13
14
15
16
17
18
19
20
21
22
23
24
25
26
27
28
29
30
31
32
33
34
35
36
37
38
39
40
41
42
43
44
45
46
47
48
49
50
51
52
53
54
55
56
57
58
59
60
39. W.-Y. Huang, G.-L. Davies and J. J. Davis, *Chem. Commun.*, 2013, **49**, 60-62.
40. J. J. Davis, W.-Y. Huang and G.-L. Davies, *J. Mater. Chem.*, 2012, **22**, 22848-22850.
41. N. Portney and M. Ozkan, *Anal. Bioanal. Chem.*, 2006, **384**, 620-630.
42. M. Norek, I. C. Neves and J. A. Peters, *Inorg. Chem.*, 2007, **46**, 6190-6196.
43. J.-L. Bridot, A.-C. Faure, S. Laurent, C. Riviere, C. Billotey, B. Hiba, M. Janier, V. Jossierand, J.-L. Coll, L. Vander Elst, R. Muller, S. Roux, P. Perriat and O. Tillement, *J. Am. Chem. Soc.*, 2007, **129**, 5076-5084.
44. J. J. Day, B. V. Marquez, H. E. Beck, T. A. Aweda, P. D. Gawande and C. F. Meares, *Curr. Opin. Chem. Biol.*, 2010, **14**, 803-809.
45. G. Zhu, M. Ye, M. J. Donovan, E. Song, Z. Zhao and W. Tan, *Chem. Commun.*, 2012, **48**, 10472-10480.
46. Z. Ali, A. Z. Abbasi, F. Zhang, P. Arosio, A. Lascialfari, M. F. Casula, A. Wenk, W. Kreyling, R. Plapper, M. Seidel, R. Niessner, J. Knoell, A. Seubert and W. J. Parak, *Anal. Chem.*, 2011, **83**, 2877-2882.

Table 1 The amount of Gd and Al in various Gd-Al@MSNs-NH₂ samples and the respective relaxation data.

Sample #	Gd (wt%)	Al (wt%)	Gd (mmol g ⁻¹)	Al (mmol g ⁻¹)	Al/Gd (m/m)	r ₁ (mM ⁻¹ s ⁻¹)	r ₂ /r ₁
1	4.52	0.943	0.287	0.350	1.22	14.2	1.3
2	4.46	0.869	0.284	0.330	1.17	12.6	2.0
3	4.03	0.801	0.256	0.297	1.16	13.9	1.7
4*	4.27	0.806	0.272	0.299	1.10	17.3	1.1
5	3.78	0.664	0.240	0.246	1.02	16.5	1.2

* The optimal Gd-Al@MSNs-NH₂ and its respective relaxation data.

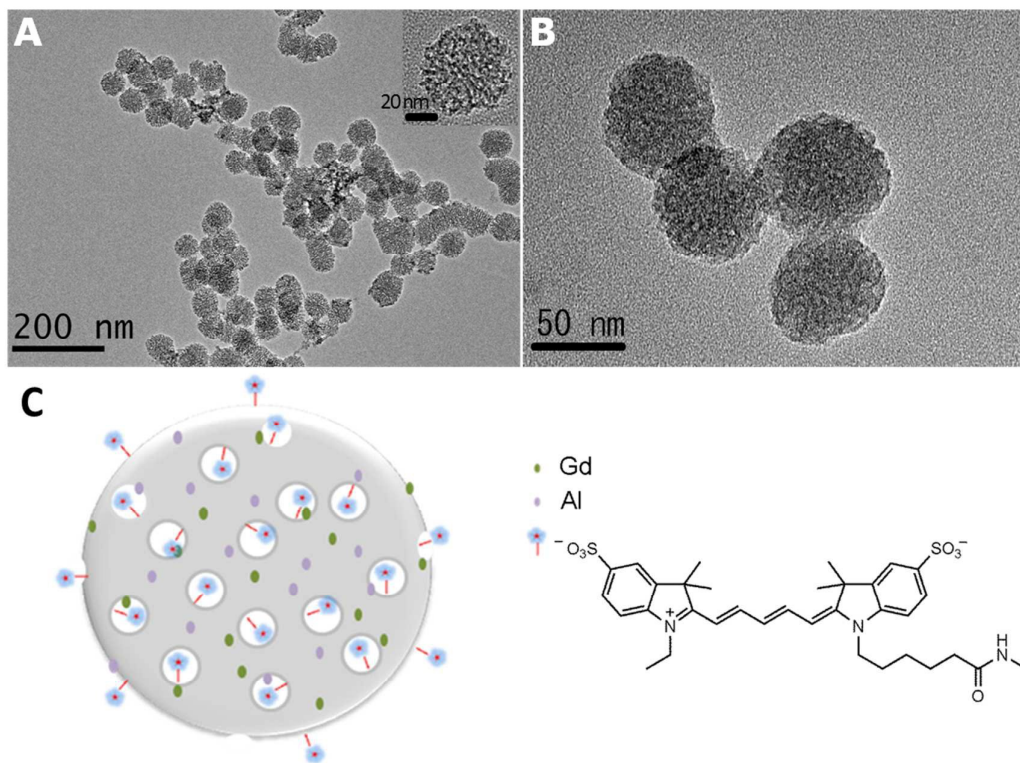


Fig. 1 TEM images of (A) Gd-Al@MSNs-NH₂ and (B) Gd-Al@MSNs-Cy5. Inset is the same sample at high resolution with 20 nm scale. (C) Illustration of NIRF-MR DMIPs of the mesoporous structure with the co-doped Gd and Al as well as the labeled Cy5.

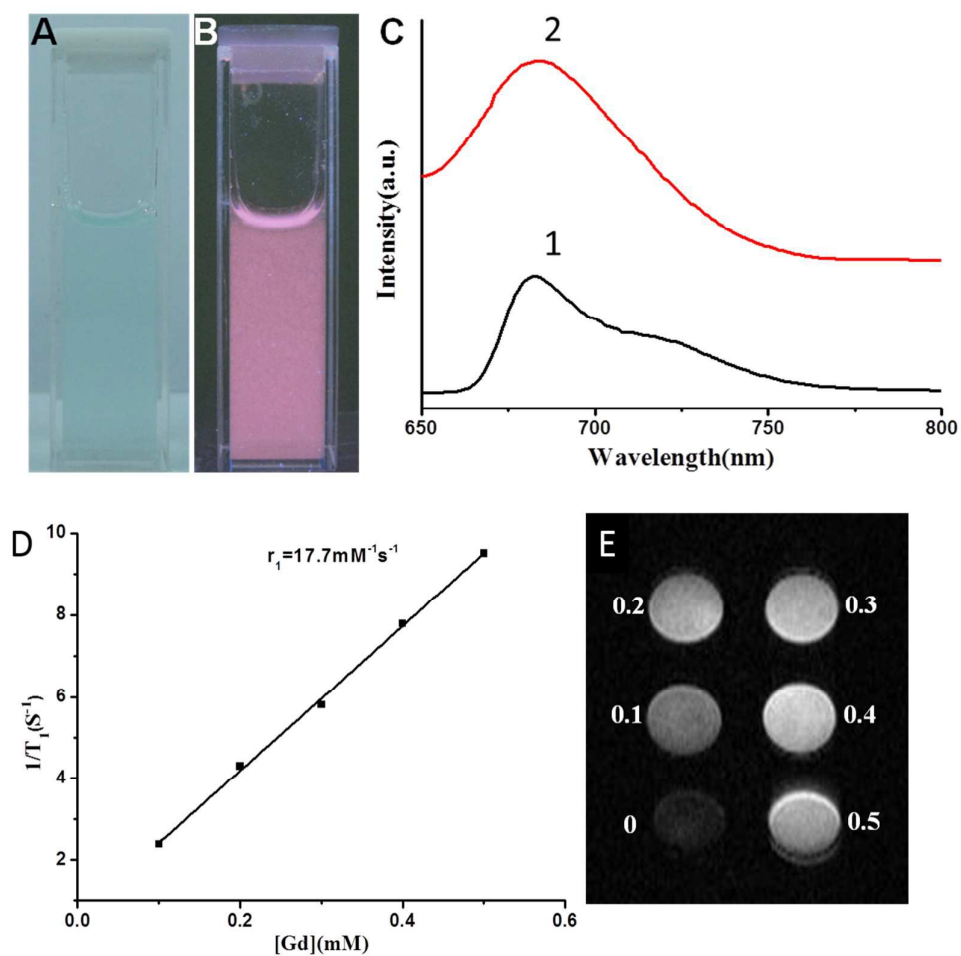


Fig. 2 Gd-Al@MSNs-Cy5 at a concentration of 1 mg mL^{-1} under (A) natural and (B) UV light. (C) The fluorescence spectrum of (1) Cy5 and (2) Gd-Al@MSNs-Cy5 at the excitation of 630 nm wavelength. (D) The r_1 relaxation curve of Gd-Al@MSNs-Cy5. (E) T1-weighted phantom images of different concentrations of Gd-Al@MSNs-Cy5.

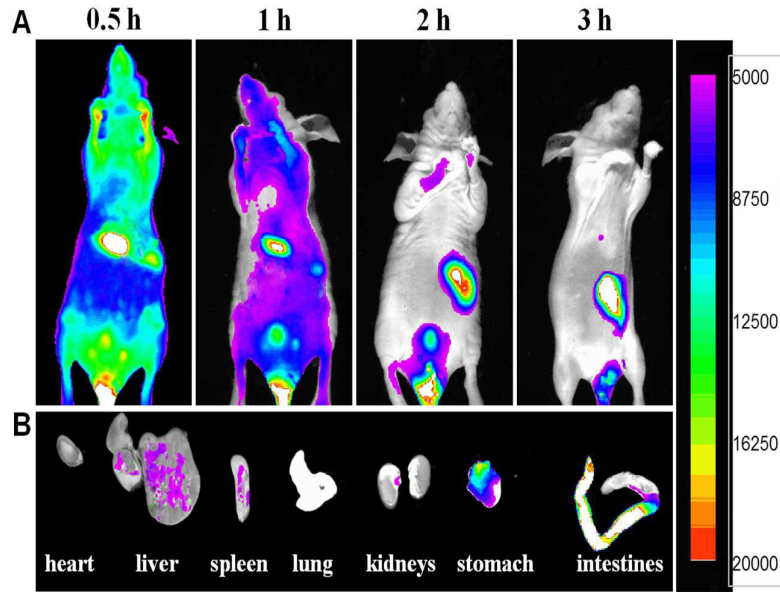


Fig. 3 (A) *In vivo* fluorescent images of mice with intravenous injection of Gd-Al@MSNs-Cy5. (B) *Ex vivo* images of resected organs at 3 h after injection.

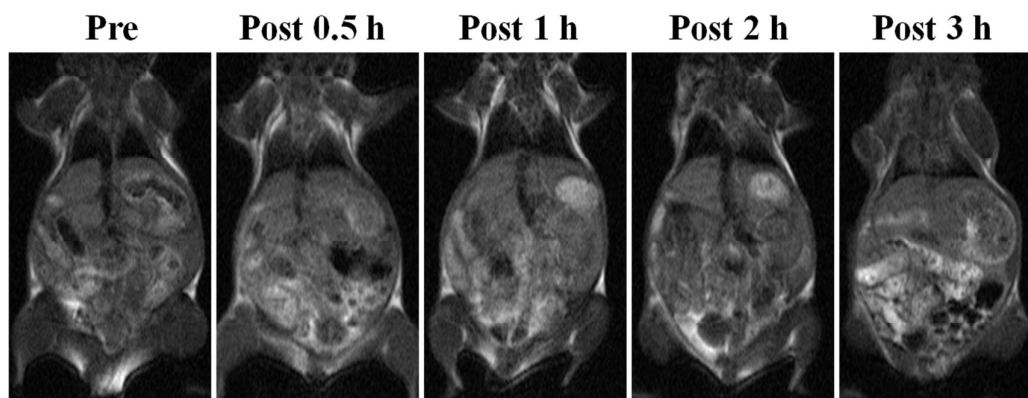


Fig. 4 *In vivo* MR image of mice with intravenous injection of Gd-Al@MSNs-Cy5.

Table of Contents

We report a reliable and facile procedure to prepare near infrared fluorescence (NIRF)-magnetic resonance dual-modal imaging probes (DMIPs) using Cy5-labeled, Gd-Al co-doped mesoporous silica nanoparticles. High intensity of NIRF and relaxation rate ($17.7 \text{ mM}^{-1}\text{s}^{-1}$) can be observed. Furthermore, the DMIPs in saline were injected into mice through tail vein for imaging and basic pharmacokinetics study.

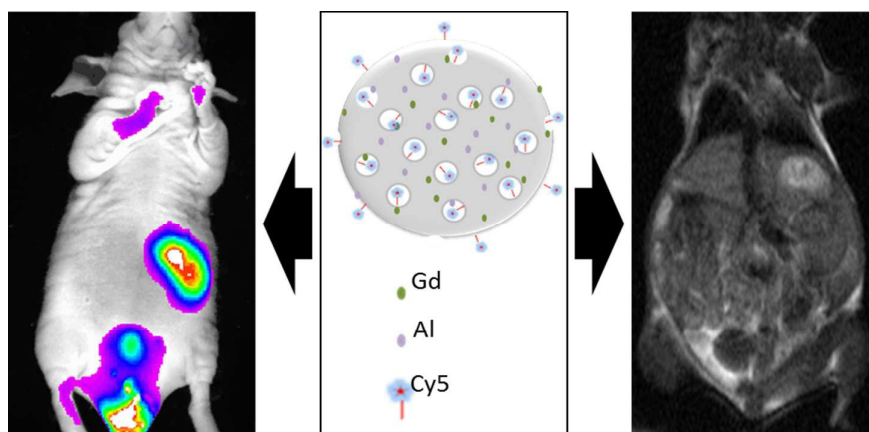


TABLE OF CONTENTS

NIRF-MR imaging is reported with Cy5-labeled, Gd-Al co-doped mesoporous silica nanoparticles.

We report a reliable and facile procedure to prepare near infrared fluorescence (NIRF)-magnetic resonance dual-modal imaging probes (DMIPs) using Cy5-labeled, Gd-Al co-doped mesoporous silica nanoparticles. High intensity of NIRF and relaxation rate ($17.7 \text{ mM}^{-1}\text{s}^{-1}$) can be observed. Furthermore, the DMIPs in saline were injected into mice through tail vein for imaging and basic pharmacokinetics study.

